Materials Science in Semiconductor Processing 186 (2025) 109038

Contents lists available at ScienceDirect

Materials Science in Semiconductor Processing

journal homepage: www.elsevier.com/locate/mssp

High-pressure sputtering deposition and *in situ* plasma oxidation of TiO_x thin films as electron selective contact for photovoltaic applications

F. Pérez-Zenteno [a,*], E. García-Hemme [a], I. Torres [b], R. Barrio [b], S. Duarte [a], R. Benítez-Fernández [a], D. Caudevilla [a], R. García-Hernansanz [a], J. Olea [a], D. Pastor [a], A. del Prado [a], E. San Andrés [a]

[a] Dpto. Estructura de La Materia, Física Térmica y Electrónica, Universidad Complutense de Madrid, Fac. de CC. Físicas. Plaza de Ciencias 1, E-28040, Madrid, Spain
[b] Unidad de Dispositivos Energéticos y Ambientales, Dpto. de Energías, CIEMAT. Av/ Complutense 40, E-28040, Madrid, Spain

ARTICLE INFO

Keywords:
High-pressure sputtering
Selective contacts
Photovoltaics
Plasma oxidation
Cox&Strack method
Heterojunction solar cells

ABSTRACT

In this article, we show the structural, optical, and electrical characterization of TiO_x deposited by the unconventional technique of High-Pressure Sputtering (HPS). This technique has the potential to reduce the plasma-induced damage of the samples. To fabricate the TiO_x, a 2-step process was used. Firstly, a thin Ti film was deposited in an Ar atmosphere. Secondly, O_2 was introduced into the HPS chamber to create an Ar/O_2 plasma that, along with low temperatures (150 °C or 200 °C), induces the oxidation of the deposited Ti film. With this approach, the Ti film is expected to behave as a capping layer that will reduce the oxidation of the Si substrate. This study aims to obtain a TiO_x layer with low specific contact resistivity (ρ_c) and high minority carrier lifetime. These are crucial characteristics for obtaining high-quality selective contact. It was found that the 2-step process can oxidize the Ti layer. These HPS TiO_x layers show a resistivity in the order of 0.3–10 Ωcm and a ratio Ti/O of ~1.9. Moreover, the SiO_x regrowth is minimal since this is comparable to the native oxide. This was confirmed by transmission electron microscopy (TEM) and Fourier transform infrared spectroscopy (FTIR). The samples fabricated with a Ti layer (~4 nm) plus an oxidation temperature of 200 °C (duration of less than 2 h) show a low ρ_c of 0.02 Ωcm^2, an excellent transmittance (>87 %) in the visible region and an optical bandgap of 2.8 eV. These TiO_x layers are amorphous, although some anatase phase crystalline clusters appear for the 200 °C processes. However, the minority carrier lifetime results of Si passivated by TiO_x were inadequate for fabricating efficient solar cells. We also found that using the RCA oxide improved lifetime. This indicates that introducing alternative low-temperature passivating layers can solve this issue.

1. Introduction

Advances in single junction silicon-based photovoltaic technologies have made it possible to achieve cells with efficiencies close to the theoretical maximum (~30 % according to Shockley-Queisser limit [1]). Therefore, the current mainstream efforts lie in researching new materials and manufacturing technologies to reduce costs and environmental impact while preserving high efficiencies. In this context, heterojunction solar cells have much to offer since they allow the exploration of many materials manufactured by different methods. For instance, the most widespread silicon heterojunction structure is the well-known HIT solar cell, which includes a-Si:H(i)/a-Si:H(n/p) as passivating-selective layers. The outstanding efficiency of more than 26.81 % has been obtained with this structure [2]. However, the low bandgap of a-Si:H causes parasitic blue light absorption, which reduces the solar cell efficiency [3]. A typical 50 nm a-Si thin film only has a transmittance of ~25 % in the blue range (450–500 nm), according to Ref. [4]. Furthermore, a-Si:H(n) deposition by PECVD requires SiH_4 and PH_3, which are highly hazardous and extremely inflammable precursor gases. For that reason, the research on transition metal oxides (TMO) as alternative electron selective contact (ESC) or hole selective contact (HSC) has gathered attention due to the wide bandgap (highly transparent) and low contact resistivities when deposited using the right conditions [5]. Moreover, the temperature for depositing TMO tends to be low ($T < 200$ °C). This low deposition temperature would potentially reduce the thermal budget and hence the energetic cost of the cell

* Corresponding author.
E-mail address: francp05@ucm.es (F. Pérez-Zenteno).

https://doi.org/10.1016/j.mssp.2024.109038
Received 22 July 2024; Received in revised form 4 October 2024; Accepted 21 October 2024
Available online 29 October 2024

manufacturing route [6].

In that context, TiO_x has been recently studied as ESC in organic solar cells [7], perovskite [8] and Si/perovskite tandem solar cells [9] since it has shown excellent selectivity behavior. In fact, TiO_x has already been used in silicon heterojunction solar cells, achieving an efficiency of 20.5 % [10]. The deposition techniques that have been mostly used are atomic layer deposition (ALD) [11–13], thermal evaporation [14], e-beam evaporation [15], and spray pyrolysis techniques [8]. In contrast, sputtering has not been extensively studied since plasma is usually associated with degradation of the underlying films [16,17]. The sources of such damage may be several, although some studies have shown that this damage is actually produced not by radiation but by the collision of the sputtered species that are expelled with high-energy [18]. This energy can be reduced if the pressure of the sputtering chamber is increased. In that sense, if the pressure is increased, the mean free path of the species in the plasma and, consequently, their kinetic energy could be reduced. Under this condition, the species in the plasma would thermalize before reaching the substrate.

Following these ideas, in this work, we study the non-conventional technique of high-pressure sputtering (HPS) that allows us to work in the 0.5–5 mbar range. At these pressures, the mean free path is 10^{-2}-10^{-3} cm; therefore, the sputtered species will suffer many collisions before reaching the substrate. In contrast, at typical sputtering pressures (10^{-2} – 10^{-3} mbar), the mean free path of the species is in the order of some cm [19]. In this sense, HPS can reduce the permanent damage to the substrate or any deposited layer on top. In previous works, we have successfully used HPS for growing high-*k* dielectrics such as TiO_x [20], HfO_2 [21], Gd_2O_3 [22] and $Gd_xSc_{2-x}O_3$ [23]. For heterojunction solar cells, we have obtained promising results by depositing indium tin oxide (ITO) as a transparent conducting layer [24] and MoO_x as HSC [24]. This article will present the structural, electrical, and optical characterization of TiO_x films deposited on crystalline n-type Si by HPS. To our knowledge this is the first time that TiO_x deposited by HPS is studied as ESC for solar cell applications.

2. Experimental

Polished FZ n-Si <100> 1000–10000 Ωcm 500 μm, 1 × 1 cm^2 samples were used to measure the TiO_x sheet resistance. For the transmittance and reflectance measurements, 1 × 1 cm^2 0.7 mm thick fused quartz was used, and for the rest of the measurements, polished FZ n-Si <100> 300 μm, 1–5 Ωcm samples were employed. The Si samples were cleaned with 1 min of diluted HF for all structural measurements and then rinsed with deionized water before entering the HPS chamber. For the Cox&Strack (C&S) measurements, the samples were cleaned with the standard RCA process. Before entering the HPS chamber, the native SiO_x was removed by 1 min of diluted HF and rinsed with deionized water. For the process, the chamber was evacuated before sputtering to a base pressure of 1.4 x 10^{-6} mbar. In all cases, the samples were heated in a vacuum at 150 °C for 10 min to eliminate any residual water.

Ti films (~4 nm) were deposited by HPS from a 2″ Ti target with a pure Ar atmosphere. The deposition time for the Ti film was 6 min. Immediately, without breaking the vacuum, O_2 is introduced into the chamber to create an Ar/O_2 plasma using the same Ti target. It maintained a constant argon-to-oxygen ratio of 95 % Ar and 5 % O_2 for all the oxidation processes. This Ar/O_2 plasma produces the oxidation of the previously deposited Ti layer. There might be a small deposition of TiO_x in the oxidation step. Therefore, the final layer would comprise a plasma-oxidized Ti layer plus TiO_x on the top. According to ellipsometry measurements and TEM images, the deposition rate in this step is around 1.6 nm/h. Reduced substrate temperatures of 150 °C or 200 °C were used to facilitate the oxidation of Ti film. We did not study higher substrate temperatures to ensure a HIT-compatible route. Moreover, multiple oxidation times, i.e., when Ar/O2 plasma was located on top of the sample, were considered (0.25 h, 0.5 h, 1 h, and 2 h). The working pressure remained constant for both plasma processes at 0.5 mbar, and the net *rf* power was 45 W (reflected *rf* power below 5 W). We used a Hüttinger PFG 300 rf power source that works at 13.65 MHz, which is attached to a matchbox to minimize the reflected power. For the first step (Ti deposition), the conditioning time was around 2 h to ensure that the Ti target was not poisoned by oxygen from the oxidation step of previous processes. On the other hand, for the second step (Ti oxidation), the conditioning time was reduced to 30 min since we did not notice any change beyond this time. The plasma composition was determined by Optical Emission Spectroscopy (OES), which allowed the characterization of the species' intensity in the plasma. We use the spectrometer Blue-Wave from StellarNet for OES with a 200–850 nm wavelength range. The optical fibers were focused on the plasma core through a sapphire window to ensure UV transmittance. The following table summarizes the high-pressure sputtering and *in-situ* oxidation processes.

The TiO_x films were measured by the four-point probe to confirm that the Ti film was oxidized. For these measurements it was used high resistivity Si substrates. An automated GMT-SR2000PV system was used. The probe separation is 1 mm which is much larger than the TiO_x film thicknesses and smaller than the sample dimension. Therefore, the ideal correction factor $\pi/\ln(2)$ was used. To determine the thickness of the films, ellipsometry measuring was done with a Gaestner ellipsometer operating at 632.8 nm with a fixed incident angle of 70°. Thanks to the mapping capability of the ellipsometer, the thickness was determined statistically from maps of 169 points along the sample. For the sample fit, it was considered a simple two-layer structure: a Si substrate with fixed standard values (at 632.8 nm) of refractive index of 3.86 and extinction coefficient −0.0016 [25] and a TiO_x layer (5 nm) with a refractive index of 2.41 and extinction coefficient of 0 at 632.8 nm [26]. The fitted parameters were the thickness and refractive index of this film.

Additional measurements, such as Fourier Transform Infrared Spectroscopy (FTIR), were done to determine the bond structure of the samples. We used an FTIR spectrophotometer Nicolet iS50 measuring in the 400-4000 cm-1 range with an everGlo infrared light source, a KBr beam-splitter, and a DTGS-KBr detector. The resolution of the measurements was 16 cm^{-1} and each spectrum was averaged from 70 scans. The samples were measured in transmission. To obtain the final graphs, the n-Si reference spectrum was subtracted from the total n-Si/TiO_x spectrum to eliminate the contribution of the Si substrate.

X-ray Photoelectron Spectroscopy (XPS) measurements were performed to determine the chemical composition. For this, it was used a Fisons MT500 spectrometer equipped with a hemispherical electron analyzer (CLAM2) and a non-monochromatic Mg Kα X-Ray source operated at 300 W. The samples were fixed on small flat discs supported on an XYZ manipulator placed in the analysis chamber. The residual pressure in this ion-pumped analysis chamber was maintained below 10^{-9} mbar during data acquisition. The spectra were collected at a pass energy of 20 eV, which is typical of high-resolution conditions. Spectra were analyzed using CasaXPS software. The intensities were estimated by calculating the area under each peak after subtracting the S-shaped background and fitting the experimental curve to combine Lorentzian and Gaussian lines of variable proportions. Although specimen charging was observed, it was possible to determine accurate binding energies (BEs) by referencing to the adventitious C1s peak at 285.0 eV. The maximum allowed variation of the binding energy was ±0.2 eV relative to the value specified for the peak center. The atomic ratios were computed from the peak intensity ratios and the reported atomic sensitivity factors [27].

Grazing incidence angle X-ray diffraction (GIXRD) was used to determine the crystallinity nature of the samples. We used a Philips X'pert PRO MRD. A copper tube with a 45 kV and 40 mA power was used. In the incident optics, a parabolic mirror was used to obtain a parallel beam. A parallel plate collimator was used for the grazing incidence measurements in the diffracted beam optics. A sealed Xenon point detector was used as the detector. The measurement was

performed in the 2θ range of 20° to 90°, the 2θ step was 0.05, and the measuring time was 3s per step. To mitigate the contribution of the Si substrate, the incidence angle (ω) was kept constant at 0.5° for all the samples. Since TiO_x films fabricated at temperatures below 600 °C are more likely to grow in an anatase phase than a rutile phase, we compared the diffractogram with the many references (anatase or rutile phases) using the High Score Plus software.

Additionally, some samples were chosen to be observed by transmission electron microscopy (TEM). With these images, we sought to confirm the thicknesses of the layers and to observe the crystallinity of the samples directly. A JEOL 2100 HT model with a resolution of 0.25 nm and an operation voltage of 200 kV was used. A double-tilt sample holder was used to orient the lamella, and for X-ray energy dispersive spectroscopy (XEDS) analysis, we used an Oxford Instruments INCA microanalysis system.

Moreover, to measure the specific contact resistivity (ρ_c) of the TiO_x/n-Si junction, we fabricated C&S structures [Fig. 1 (a)]. First, we ensured an ohmic back contact with very low specific contact resistance on the rear side of the Si wafer by creating an n^{++} layer. To that end, we implanted phosphorus at an energy of 32 keV and a $4x10^{15}$ cm^{-2} dose. The implanted phosphorus was activated by rapid thermal annealing (RTA) at 1000 °C for 120 s in an Ar atmosphere. We measured this layer with the transfer length method (TLM) and obtained a specific contact resistivity of $\sim 5x10^{-4}$ Ωcm^2 (see supplementary material). The wafer was cut into square pieces of 35 × 35 mm^2 and cleaned with the standard RCA process. Before entering the HPS chamber, the native SiO_x was removed by immersion on HF (1:50) for 1 min, followed by a rinse in deionized water. As mentioned above, the TiO_x was manufactured using what we call the 2-step process from which we investigated two different oxidation temperatures (150 °C and 200 °C) and multiple oxidation times (0.25 h, 0.5 h, 1 h, and 2 h). Negative photolithography was carried out to define the circular pattern of C&S. Then, we evaporated the metal stack on the front, i.e., in the side in contact with TiO_x layer (Ti 50 nm followed by Ag 100 nm) and the back contact (Ti 50 nm followed by Al 100 nm). Finally, we measured the current-voltage (IV) curves of the C&S structure and fitted the data with the traditional C&S method. For the C&S analysis, we consider the recommendation of B. van Wijngaarden et al. [29], i.e., the diameter of the circles must be smaller than two times the thickness of the substrate. In this study, the contact diameter was below 400 μm for all the samples. This is important to ensure that the contribution of the spreading resistance Rs does not hide the contribution of contact resistance. This issue is often neglected in other works and leads to a ρ_c underestimation [28]. The resistivity of the wafers was between 1 and 5 Ωcm, which is typical for commercial cells and is also adequate to measure low specific contact resistivity ρ_c. The IV curves were measured with a Keithley 2636A source and measure unit (SMU) connected to the needle probes by triax cables with a four-wire configuration.

Finally, we fabricated the structure depicted in Fig. 1 (b) to measure the minority carrier lifetime. To make the final structure compatible with the manufacturing process of a HIT cell, firstly, we deposited an a-Si:H stack on the rear side. The a-Si:H(i)/a-Si:H(n) stack has a combined thickness of ~15 nm. When this a-Si:H stack is deposited on both sides, we obtained minority lifetimes >1 ms. On the front side, a 2-step process TiO_x film was deposited following the same temperatures and oxidation times as we did to fabricate the C&S structure. Since the a-Si:H stack shows a high minority carrier lifetime, the TiO_x film will essentially determine the minority carrier lifetime limit that we could measure. These samples were measured with a Sinton WCT-120 and the results were obtained with the quasi-steady state photoconductance (QSS-PC) mode. For the measurements, the TiO_x side was facing the flash lamp of the Sinton equipment.

3. Results

For all the HPS processes, we analyzed the plasma with OES to ensure the reproducibility of the TiO_x fabrication. Fig. 2 depicts the OES spectrum for the Ar plasma, i.e. the Ti deposition step (black curve) and the Ar/O_2 plasma oxidation step (red curve). Within the Ar plasma spectrum, we can notice the presence of intense emission peaks between 200 and 600 nm that correspond to Ti extraction [29]. Besides, as it was expected, some peaks that are related to ionized Ar are present in the 700–850 nm range [29]. On the other hand, the peaks of extracted Ti almost disappeared during the oxidation process. Also, some small peaks around 394 nm appear related to oxygen presence [30]. This effect has been commonly observed when O_2 is introduced into the sputtering chamber, and it is referred to as target poisoning [31]. The reason for this effect is that ionized oxygen bonds with the Ti target, thus creating a TiO_x layer on the surface. To some extent, this dielectric layer hinders the extraction of Ti but allows the creation of a plasma that facilitates the oxidation of the previously deposited Ti layer. From an industrial standpoint, target poisoning would reduce yield due to the need for cleaning between steps. However, its impact could be avoided by using two different chambers (both with a Ti target, the first working in the regular regime and the second working in a poisoned regime). In our research system, the poisoned layer must be eliminated before the next Ti deposition process. In any case, as we can notice from the inset, when O2 is introduced to the chamber, there is still a reduced Ti/TiO_x extraction that may increase the final thickness of the TiO_x film.

To verify that the Ar/O2 plasma fully oxidized the deposited Ti film, we measured the resistivity of the samples. First, some samples with the as-deposited Ti film (i.e., without intentional oxidation) were measured.

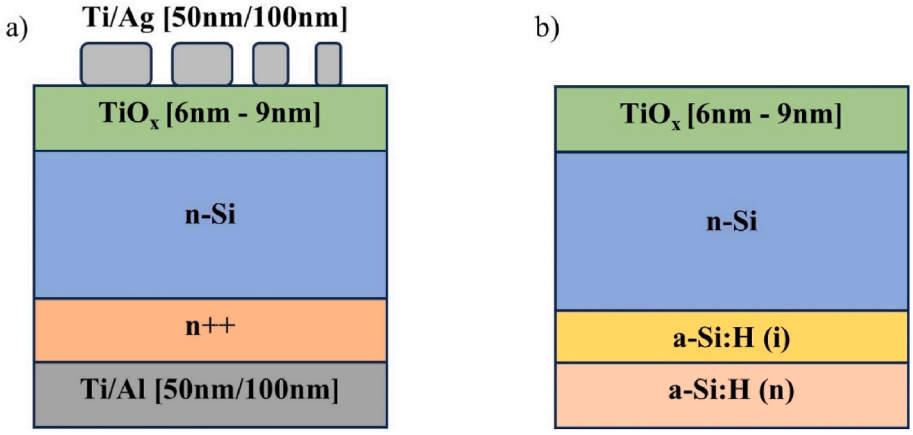

Fig. 1. a)Cox&Strack structure fabricated to measure the contact resistivity of the n-Si/TiOx interface. b) structure fabricated to measure the passivation behavior of HPS TiOx deposited on n-Si.

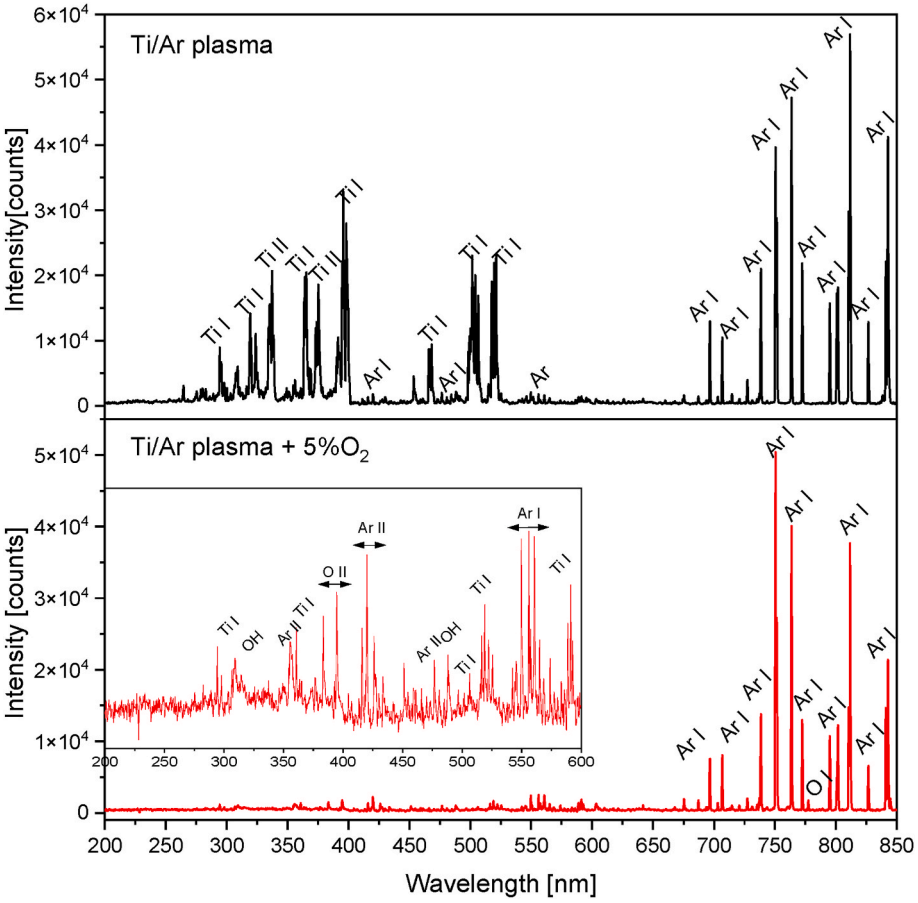

Fig. 2. Optical Emission Spectroscopy (OES) spectrum for the 2-step process of depositing TiOx thin films. The black curve is the plasma observed when the Ti is deposited. The red curve is the plasma observed during oxidation (Ar/O_2 plasma). The red curve inset is a zoom for the peaks observed in the 200–600 nm range.

The thickness of the Ti film was approximately 4 nm. We obtained a resistivity of ~$3.7x10^{-4}$ Ωcm that is within the range of Ti thin films deposited by sputtering [32]. Subsequently, we measured the sheet resistances of the samples with the 2-step process TiO_x. As depicted in Fig. 3, we notice that the resistivity for these samples increases by more than 3 orders of magnitude. This confirms that the original Ti film has been oxidized. The resistivity of stoichiometric TiO_x is extremely high, typically above 10^8 Ωcm. Nevertheless, it has been found that sub-oxidized TiO_x has a much lower resistivity in the range of 0.26 Ωcm to 10 Ωcm [33,34], which is congruent with our results.

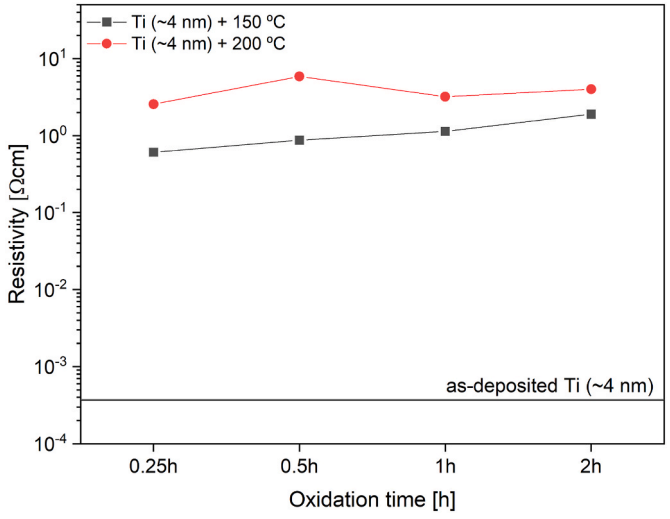

Fig. 3. Resistivity of TiO_x thin films deposited by HPS with the 2-step process oxidation. Two different oxidation temperatures are considered (150 °C and 200 °C). The reference line is the resistivity we found for the Ti film deposited during 6 min (~4 nm).

To measure the chemical composition of these samples, we performed XPS analysis. No surface cleaning by sputtering was performed during the measurement, so the results came solely from the top surface of the films. Fig. 4 depicts the preliminary scan data of the samples. It is noticeable that the intensity of the O-1s peak increases when plasma oxidation processes take place. Furthermore, as it is commonly observed, emission from C-1s is present due to the handling of the samples and air exposure [35]. The samples had to be removed from the HPS chamber and transported to another laboratory for XPS measurement.

In Table 2, we show the concentrations of the main atomic species present in the surface obtained by peak fitting (see Table 1). We measured a high amount of organic contamination, which is almost inevitable when the samples are measured ex-site by XPS. If we obtain the O/Ti ratio directly from the integrated areas of Ti and O, as shown in Table 2, the values are overestimated since they are higher than 2.5 in all samples. This indicates that a huge part of the oxygen signal comes from surface contamination. To remove this contamination, an in-situ sputter clean could be used. The system used for the measurements did not have this tool available. Also, with this sputtering cleaning process, the chemical bond structure of the Ti-O bonds could be influenced seriously, reducing the oxidation state of Ti. Thus, to estimate the O/Ti ratio x, we have calculated this parameter assuming that titanium is bonded only to oxygen, and the amount of bonded oxygens is given by the Ti oxidation states.

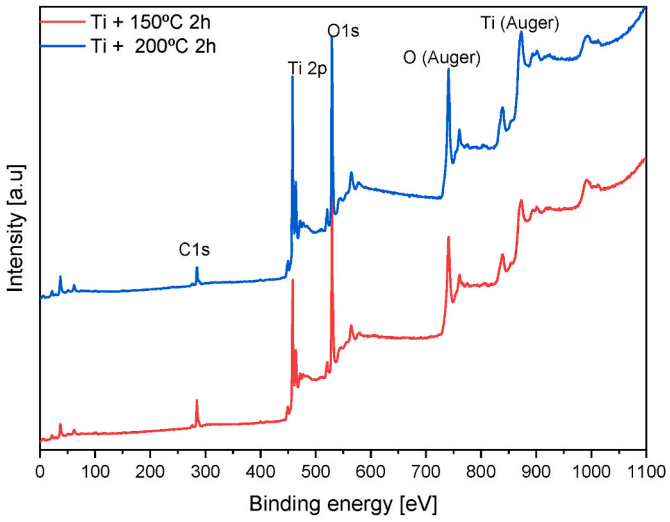

Fig. 4. XPS scan spectra for the as-deposited Ti and Ti oxidized with the O_2 plasma at 150 °C and 200 °C.

Table 1
Summary of the 2-step process to fabricate TiO_x layer by HPS with an in-situ plasma oxidation process.

Process step	Details
Si sample pre-cleaning	RCA1 + RCA2 + HF (5 %) + deionized water
Pre-heating of the substrate holder	Time: 10 min Temp.: 150 °C
Target conditioning 1 (Ar)	Initial pressure: ~10^{-6} mbar 0.5 mbar, 50 W Time: ≤2 h Temp.: RT
Ti deposition (~4 nm)	0.5 mbar, 45 W Time: 6 min Temp.: RT
Target conditioning 2 (Ar + O_2)	0.5 mbar, 45 W, 5 % O_2 Time: ≤30min Temp.: RT
Oxidation process	Time: 0.25 h, 0.5 h, 1 h, or 2 h Temp.: 150 °C or 200 °C

In Fig. 5 we depict the deconvoluted XPS peaks for the Ti-2p and O-1s emissions. These results show that the Ti film was effectively oxidized by the plasma treatment sample, but they are sub-stoichiometric, as the presence of titanium suboxides (Ti^{+2} and Ti^{+3}) indicates. Concerning the O-1s peak, a shoulder is present. This is commonly referred to as oxygen vacancies (O_v) and suggests the formation of oxygen vacancies in the lattice [36]. Nevertheless, the lattice oxygen (O_L) in the O-1s peak is predominant in these samples. For the 150 °C 2 h sample, the O_L represents 72.5 % of the total O-1s peak while O_v is 27.5 %. Meanwhile, for the 200 °C 2H samples, O_L is 78.4 %, and O_v is 21.5 % of the total O-1s peak. We can conclude that the percentage of O_L will increase with a higher temperature for the oxidation process. This means that the oxygen vacancies bond with other atoms in the lattice, thus stimulating the formation of Ti-O bonds. The x value of TiO_x was calculated considering the relative height of the Ti^{+4} peak with respect to the rest of the oxidation states (i.e., Ti^{+3} and Ti^{+2}). As it can be seen in Table 2 The ratio O/Ti for the 150 °C 2 h sample is 1.96, and for the 200 °C 2 h sample is 1.93. The main conclusion is that the two-step HPS process yields sub-stoichiometric TiO_x films.

One of the main reasons for performing the 2-step deposition process is to control the oxidation of the Si substrate. For that, the Ti thin film deposited on the first step acts as a capping layer. Other works showed that the direct deposition of TiO_x on Si can trigger the growth of thick interfacial SiO_x [20]. If the SiO_x film is thicker than 2–3 nm, this could severely affect its use as ESC due to increased cell series resistance. FTIR measurements were performed to understand better the chemical bonds and the possible growth of SiO_x in our samples. The results are shown in Fig. 6. This figure shows 3 different FTIR spectra for 150 °C oxidations and 3 spectra for 200 °C. We also fabricated samples using only the oxidation process, i.e., the Ar/O2 (1-step process), to compare with the samples using the Ti as a capping layer (see supplementary material). The Si-O bond (stretching) is normally found in the 932-1082 cm^{-1} range. The stoichiometric SiO_2 vibration is located at 1082 cm^{-1} [37]. It is noticeable that with the samples fabricated with the 2-step process, there is not an appreciable growth of SiO_x. This means that the SiO_x thickness after the process is comparable with the native SiO_x of the reference substrates, which are also HF cleaned before measurements. On the other hand, for the 1-step process samples (orange curve), a broad peak centered in 1050 cm^{-1} is found, which confirms that the Si substrate has been oxidized to some extent. This indicates that the Ti film (~4 nm) efficiently acts as a capping layer. Concerning Ti-O bonds, in the samples oxidized at 200 °C, we can observe peaks at 420 cm^{-1} and 470 cm^{-1}. These can be attributed to Ti-O bending in anatase structure [38] and Ti-O stretching [39], respectively. However, the samples oxidized with 1 h and 0.5 h appear to have a broader peak around 435 cm-1, which is normally referred to as anatase TiO_x [40]. This can be explained by the lower process temperature and a shorter oxidation time which does not allow the complete formation of anatase structure, thus showing broader FTIR peaks.

To determine whether the samples presented a certain crystallinity, we measured the samples by GIXRD. Fig. 7 shows the diffractograms for the samples oxidized at 200 °C (0.5 h, 1 h, and 2 h), the as-deposited Ti (~4 nm), and the Si substrate. The patterns best fitting our diffractogram were ICSD 01-070-6826 and ICSD 01-086-4330 (anatase TiO_x). We can observe the presence of a broad peak around $2\theta = 55°$ for all the samples. This has been frequently observed when Si (100) substrates are measured with GIXRD. At certain azimuth angles of the samples with respect to the detector, it can be observed the (113) Si plane, which corresponds to $2\theta = 56.4$ [30,41]. This broad peak is also present in the diffractogram of the bare Si sample, so we can confirm that it is partly due to the Si substrate and will not be discussed further. Moreover, the (211) plane of the TiO_x in the anatase phase is also usually found at 56°. The GIXRD results show an increase of the intensity in the 54-56° region with oxidation duration, so we are likely observing the diffraction of both the Si substrate and the TiO_x film in this range. Also, as was expected, the as-deposited Ti sample is practically the same as the Si substrate. This shows the amorphous nature of the sputtered Ti layer.

On the one hand, for the case of the 150 °C samples, no appreciable difference was observed as we increased the plasma oxidation time. On the other hand, the samples that were oxidized at 200 °C are depicted in Fig. 7. The plane (113) of Si is again observed for all the oxidation times. However, as oxidation time increases, a peak at $2\theta = 56°$ becomes more relevant. This can again be related to the formation of the (211) plane of

Table 2
The atomic percentages of O, C, Ti, and Ti oxidation states found in the samples by XPS. The Ti/O ratio is calculated by the areas of the Ti and O.

Oxidation process	% of total			x (O/Ti)	Oxidation states of Ti			x (Ox. states)
	O	C	Ti		Ti^{+4}	Ti^{+3}	Ti^{+2}	
150 °C 2h	54.8	24.1	21.1	2.60	19.39	1.46	0.65	1.96
200 °C 2h	56.9	18.5	24.6	2.51	22.19	1.57	0.86	1.93

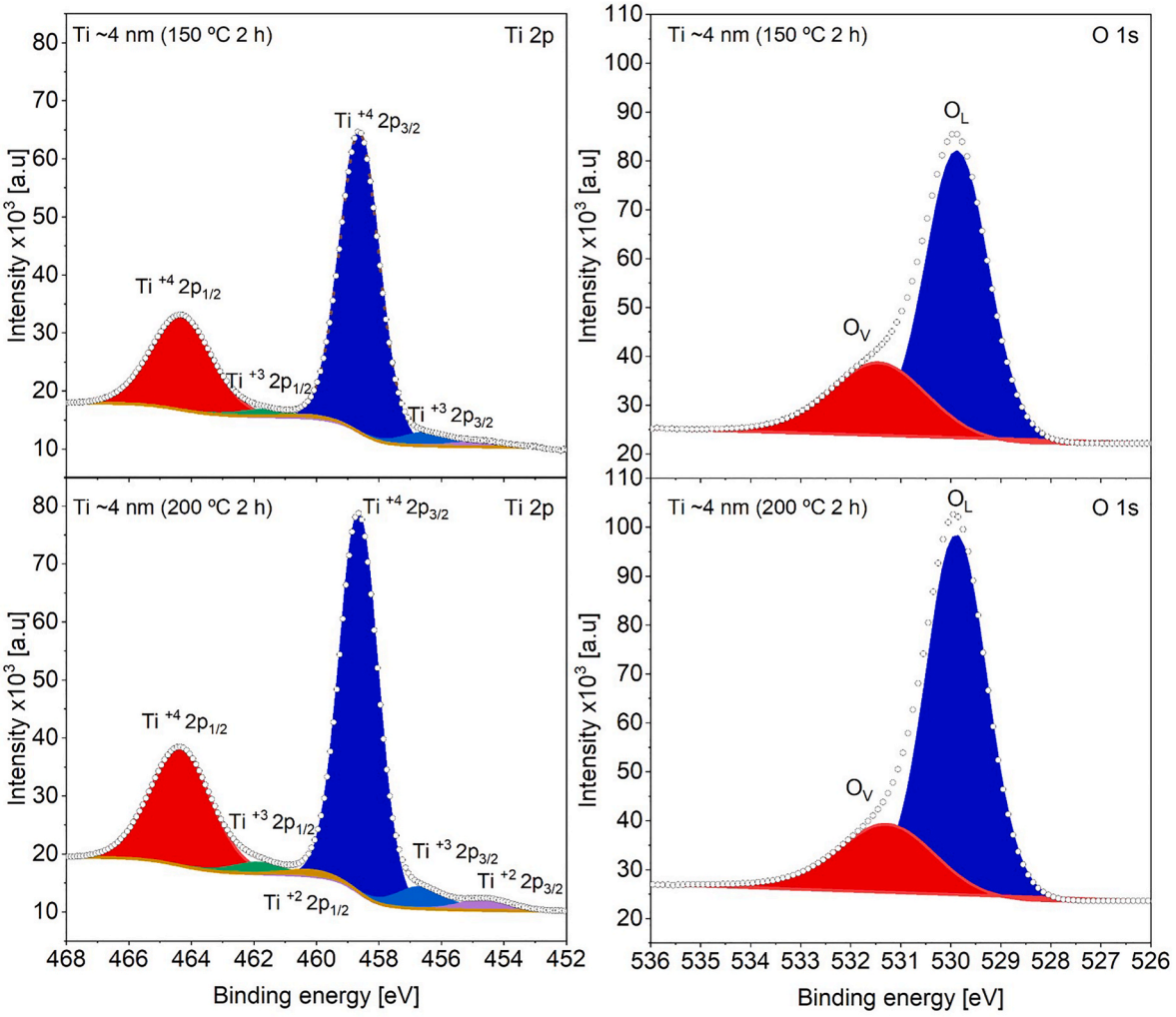

Fig. 5. XPS spectra for the Ti-2p (a) and O-1s (b) emission peaks for Ti as-deposited and for Ti oxidized with the O_2 plasma at 150 °C and 200 °C.

TiO_x in the anatase phase [42]. Finally, in the case of the sample oxidized at 200 °C for 2 h, a small peak at 81° is observed, which might indicate (008) anatase TiO_x planes. This information shows that the samples oxidized at 150 °C do not present a high degree of crystallinity. Nevertheless, the 200 °C samples show anatase phase planes which become more noticeable as the oxidation time increases. This is in accordance with the minimum temperature (~200 °C) necessary to observe the anatase phase of TiO_x [26].

One of the most important parameters to determine whether a material can be used as ESC is the specific contact resistivity ρ_c. Therefore, we fabricated C&S structures (Fig. 1 (a)) to measure the ρ_c of the Ag/Ti/TiO_x/c-Si stack. Due to the relevance of these measurements and following the guidance of the physical characterization previously presented, we have varied the deposition time (6, 4, and 2 min) of the Ti capping layer for this set of devices. Again, 150 °C and 200 °C were the oxidation temperatures we used. The oxidation process durations were 0.25 h, 0.5 h, 1 h and 2 h. The IV curves were measured between −1 V and 1 V. However, to determine the total resistance, we analyzed the result in the −0.05 V–0.05 V range to ensure a lineal behavior to use the traditional C&S method. We used the following expression to analyze the results:

$$R_T - R_S = \frac{\rho_c}{\frac{1}{4}\pi d^2} + R_O \qquad 1)$$

Where ρ_c is the specific contact resistivity, d is the contact diameter, R_O is the rear contact resistance, R_T is the total resistance measured, and R_S is the spreading resistance of the substrate. The following expression expresses this

$$R_S = \frac{\rho_w}{\pi d} arctan\left(\frac{4t}{d}\right) \qquad 2)$$

Where ρ_w is the resistivity of the wafer and t is the thickness of the wafer. Finally, the value of ρ_c was obtained by fitting the RT-RS vs 1/area curve with a linear regression. This expression is the most used when C&S measurements are performed. Other expressions have been proposed to match the spreading resistance better [43]. However, for the sake of simplicity, the previous expression is still considered valid if the condition of having a contact diameter of less than 2 times de thickness of the wafer is fulfilled. We used contacts in the 90–400 μm range for this work. Furthermore, we have ensured minimal lateral conduction as we have obtained high sheet resistance on the TiO_x layer. This is extremely important since the C&S method relies on the three-resistor approach, where only transversal conduction is expected.

For instance, Fig. 8 shows this fit for a device where ~4 nm Ti was deposited (i.e., 6 min HPS deposition) and oxidized during 1 h with 200 °C. From the slope, we obtain the ρ_c (0.014 ± 6.9x10-4 Ω cm^2, in this example), and from the y-intercept, we extract the rear contact resistance (8 ± 2 Ω).

In Fig. 9, we show the summary of the C&S results for all the

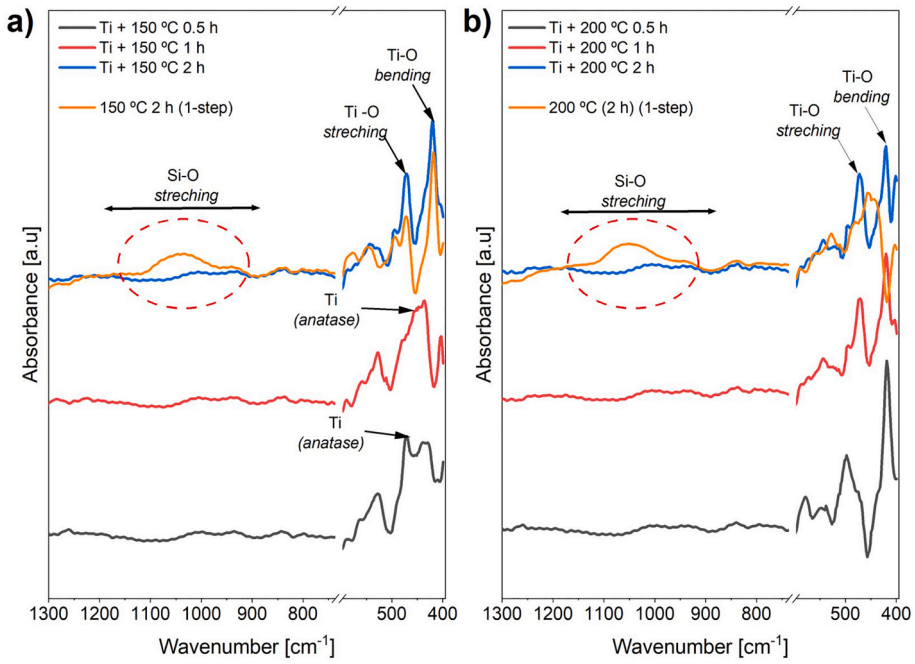

Fig. 6. FTIR spectra without the Si substrate. a) Samples fabricated with an oxidation process of 150 °C). b) samples fabricated with an oxidation process of 200 °C. For both cases, the orange curve shows the FTIR for the 1-step deposition of TiO_x at 150 °C 2 h or 200 °C 2 h.

measured samples. Several clear tendencies are noticeable. The samples with the thinner Ti capping layer (~1 nm) have a ρ_c really high, in the 10^2–10^4 Ω cm^2 range. This could be explained by the fact that the Ti film is so thin that it allows the interaction of the oxygen with the substrate, thus forming a thick SiO_x interfacial layer. On the other hand, samples with ~2.5 nm Ti have values in the range between 10^2 and 100 Ω cm^2. For this case, the samples oxidized at 200 °C present higher values, most probably because the temperature facilitates a greater oxygen diffusion to the substrate, thus forming a thicker interfacial SiO_x. Finally, the best results were obtained with samples with a Ti capping layer of ~4 nm. No significant differences were observed between the samples oxidized at 150 °C and those at 200 °C. On average, the specific contact resistivity ρ_c values were 0.03 ± 0.02 Ω cm^2. This is within the same order of magnitude as the lowest values found for the TiO_x(ALD)/c-Si interface. For instance, Ref. [44] shows a ρ_c value of 0.06 Ω cm^2 after a 500 °C 1 min annealing for the TiO_x (ALD)/SiO_x/c-Si structure, and ref [45]

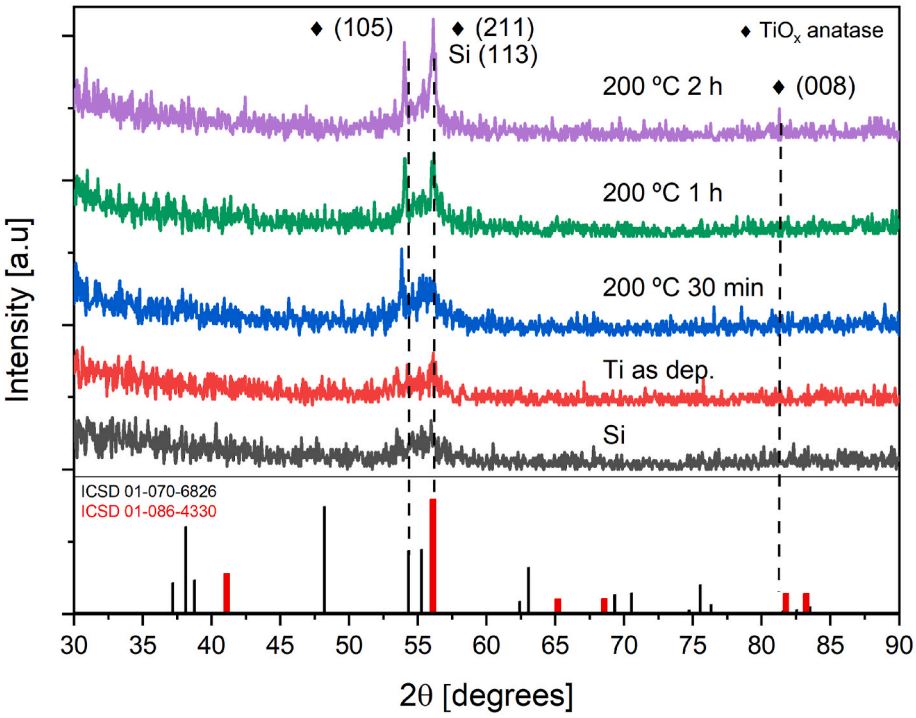

Fig. 7. Diffractograms of the Si substrate, the as-deposited 4 nm Ti, and the 200 °C oxidized samples. The ICSD 01-070-6826 and 01-086-4330 pattern of TiO_x anatase is included as a reference.

shows 0.04 Ω cm^2 for the TiO_x (ALD)/c-Si heterojunction. The only exception is the sample that was oxidized at 200 °C for 2 h, where we observed that the contact resistance increased again to 18 ± 1.6 Ω cm^2.

In summary, a direct relationship has been found between the thickness of the Ti capping layer, the oxidation process, and the contact resistivity we obtained. The crystallinity of the TiO_x does not have a strong impact on the contact resistivity. The lowest ρ_c was obtained for the ~4 nm Ti capping layer with moderate oxidation between 150 °C and 200 °C for less than 2 h. Thicker TiO_x films were not investigated since a higher series resistance was expected.

Once the best conditions to minimize contact resistivity from C&S measurements were determined, we performed TEM characterization to gain insights into the physical mechanisms that impact resistivity. We fabricated lamellas of samples deposited with some representative conditions of the 2-step process. Fig. 10 (a) shows one sample with a 150 °C 0.5 h oxidation process (minimal contact resistivity). In contrast, Fig. 10 (b) shows the sample with a 200 °C 2 h oxidation process (increased resistivity).

After the diluted HF cleaning process, a small SiO_x layer still appears for both samples. For the 150 °C 0.5 h sample, approximately 1.5 nm SiO_x is observed. Whereas, for the 200 °C 2 h samples, a slightly thicker SiO_x of 2 nm is observed. Two possible causes can explain the increase. First, the cleaning hood is a few meters away from the sputtering chamber, thus a few nanometers can regrow in contact with the atmosphere. Second, since both samples had the same starting Ti thickness, and the oxidation state is similar for both temperatures (as XPS showed), this thickness difference's origin must be the oxidation step's duration. OES shows that after O_2 introduction, there was some reduced Ti extraction, but reduced as compared to the pure Ar plasma. Thus, the second process oxidizes and deposits TiO_x at the same time. An estimation of the TiO_x deposition rate can be obtained from these TEM images. Since the TiO_x thickness difference is 2.4 nm and the oxidation duration difference is 1.5 h, thus the deposition rate can be estimated as 1.6 nm/h. This estimation assumes that the only difference between samples is the oxidation time. This is not completely true since the oxidation temperature is slightly different (150 °C and 200 °C). However, we do not expect this small temperature difference to impact the TiO_x deposition rate strongly. In any case, this rate estimation shows that the deposition rate is very low during the oxidation process.

From Figs. 9 and 10, we can deduce that this increase of the TiO_x thickness does not strongly impact contact resistivity, as Fig. 9 shows when comparing the results for 4 nm and the different oxidation times for 150 °C and 200 °C. The increase in oxidation time produces a thicker

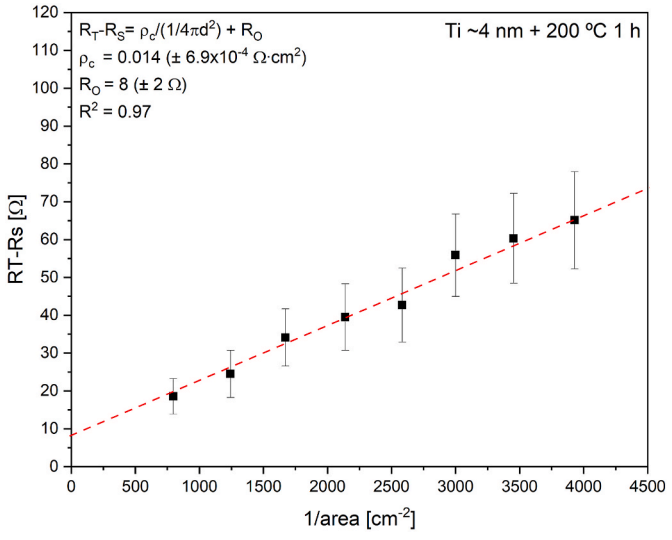

Fig. 8. Typical RT-RS vs 1/area fitting curve to obtain the specific contact resistivity using the traditional Cox&Strack method.

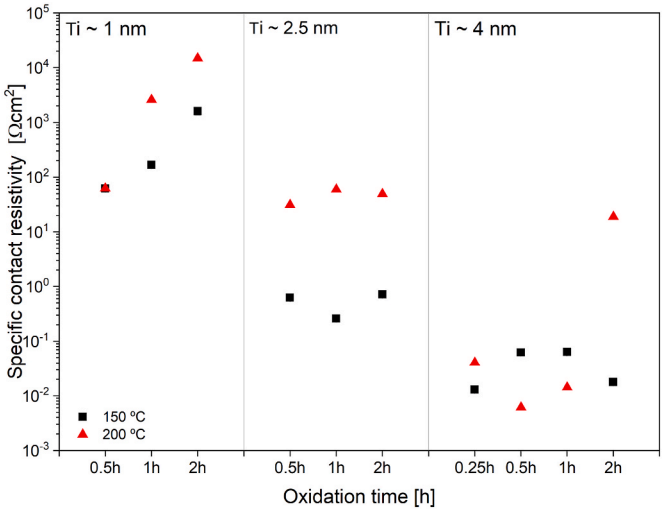

Fig. 9. Specific contact resistivity of TiO_x as a function of oxidation time. The black squares are the samples oxidized at 150 °C and the red triangles at 200 °C. Three different Ti (capping layer) thicknesses were analyzed (1 nm, 2,5 nm, and 4 nm).

TiO_x, but the specific contact resistivity remains low. Only the sample oxidized at 200 °C during 2 h shows increased contact resistivity. These conditions (higher oxidation temperature and duration) increase interfacial SiO_x thickness up to 2.2 nm. We can interpret these results as follows, for low interfacial SiO_x thickness, transport is limited by electron tunneling through this layer. Once electrons cross this layer, they are injected into the TiO_x conduction band, and the transport is only limited by their mobility in TiO_x. On the other hand, when the oxidation is performed at conditions that produce an interfacial SiO_x thickness above ~2 nm (such as Ti 4 nm, 200 °C, and 2 h oxidation), the tunneling probability decreases exponentially, and thus, specific contact resistivity increases. Fig. 9 indeed shows an increase in specific contact resistivity for the 200 °C 2 h oxidized sample with a Ti capping layer of 4 nm. However, for samples that underwent less extreme oxidations, it is not as clear that the TiO_x thicknesses have changed significantly since we do not have the TEM images. We believe that once electrons enter the conduction band of TiO_x, thickness is not as crucial. Still, the thickness of the SiO_x, which the electrons must tunnel through, is far more important and could explain increases in specific resistivity with the variations in thickness.

Although the Ti layer acts as a capping layer for the SiO_x regrowth, our results show that an extended oxidation process can oxidize the Si substrate further and thus thicken the SiO_x. This can be seen indirectly in Fig. 9, where a thinner Ti capping layer was used with the same oxidation processes. As this capping layer gets thinner, more oxygen is diffused into the Si, forming a thicker SiO_x and thus increasing the contact resistivity. On the other hand, given the good conduction band alignment of TiO_x and n-Si [ref], the increase in the TiO_x thickness should not affect the total resistance much, so the increase in 2.4 nm should not have a strong impact.

Finally, it is noticeable in the 200 °C samples that some crystalline structure appears on the surface. This can be observed with the diffraction pattern in the inset of Fig. 10 (b). From this, we obtained an interplanar distance of 0.19 nm. This agrees well with the interplanar distance obtained by GIXRD of the 211 TiO_x anatase plane, which is 0.16 nm. The presumably low rate of Ti/TiO_x deposition in conjunction with the temperature of 200 °C could have led to the formation of this crystalline arrangement.

Regarding the XEDS analysis (supplementary material), the TiO_x layer shows Ti emission lines at 4.5 and 4.9 keV in both samples. These belong to Ti K_α and Ti K_β, respectively. A weak Ti peak appears at ~0.4 keV, corresponding to Ti L_α. As expected, the O peak is also presented at

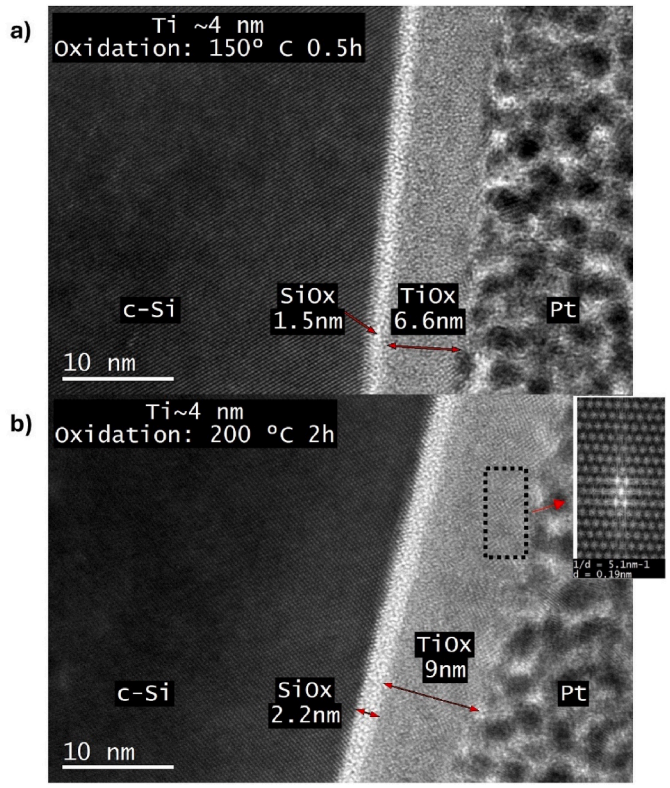

Fig. 10. a) Cross-TEM images for TiO_x samples fabricated with 150 °C 0.5 h, b) cross-TEM images for TiO_x samples fabricated with 200 °C 2 h, the inset is the diffraction pattern of the surface of the TiO_x.

0.5 keV, which is related to O K_α [46]. The presence of the Si peak is due to the spot dimension (~1 nm), which is in the same order as the TiO_x thickness. Therefore, when the spot was placed on the TiO_x layer, part of it excites on the SiO_x or even in the Si. Thus, the Si peak appears. In summary, the most important conclusion that these results show is that to obtain a low specific contact resistivity, it is necessary to avoid the regrowth of the SiO_x above 2 nm. Thus a 2-step TiO_x deposition process with an oxidation of 150 °C or 200 °C for 1 h are both good options.

Another important characteristic to consider for solar cell applications is the optical properties of the thin film. To that end, we measured the transmittance and reflectance of TiO_x films deposited on a quartz substrate. The absorptance was calculated with the $A(\lambda) = 1 - T(\lambda) - R(\lambda)$ expression. The results are shown in Fig. 11 (a).

For the samples oxidized at 150 °C, it is noticeable that as the oxidation time increases, the transmittance in the visible range (380–700 nm) increases from 83 % to 90 %. The reflectance remains constant at 8 % for the three oxidation times, and thus absorptance is reduced from 8 % to 2 %. For the samples oxidized at 200 °C, a similar behavior is observed. The transmittance varies from 87 % to 90 %, the reflectance remains at 9 %, and thus, the absorptance is maintained at around 2 %. The increase in transmittance with longer oxidation times and higher oxidation temperature may be related to the oxidation of residual Ti clusters that are not fully oxidized with a softer process. In other words, the oxygen content in the film enhances transparency. Moreover, the optical band gap was calculated through the Tauc plot [47]. To calculate the absorption coefficient α, we used the expression for the Beer-Lambert law which is normally used for thin films [16].

$$\alpha(h\upsilon) = \frac{1}{t}\ln\left(\frac{1}{T(h\upsilon)}\right) \quad 3)$$

Where t is the film thickness, $T(h\upsilon)$ is the transmittance data measured from the spectrophotometer and $\alpha(h\upsilon)$ is the absorption coefficient. With α we calculated the optical band gap with the relationship $\alpha(h\upsilon)*h\upsilon \propto (h\upsilon - E_{gap})^{,2}$, which is commonly used to determine the band gap of amorphous/polycrystalline semiconductors with indirect interband transitions [48]. Fig. 12 (b) depicts the Tauc plot for the 150 °C and 200 °C samples. The samples oxidized at 150 °C show an increase in the band gap from 2.67 eV for the shortest oxidation time to 2.88 eV for the longest, consistent with the absorptance trend. Meanwhile, the 200 °C samples do not show an important bandgap change (2.88 eV for 0.5 h and 2.89 eV for 2h). The optical bandgap of stoichiometric TiO_2 (calculated by Tauc's plot) is reported to be around 3.2 eV [47]. Nevertheless, other works have shown that O_2 vacancies inside the TiO_2 can reduce the bandgap between 2.7 eV and 3.2 eV [49]. We have measured an optical bandgap that is below the stoichiometric value for all samples, and the bandgap increases with extended plasma duration or higher plasma temperature. Thus, these trends suggest that the samples have fewer oxygen vacancies as the oxidation process is more aggressive. The reduction of the TiO_x bandgap has been proven to occur when O_2 vacancies are presented in the film [50,51]. O_2 vacancies create donor levels, while Ti vacancies create acceptor levels. These donor and acceptor levels within the bandgap are de origin of the reduction of the bandgap [52]. Higher oxidation temperatures can produce stoichiometric films (with an increase in the band gap) but at the cost of affecting the Si substrate and producing a thicker interfacial SiO_x. As our results show, this would be detrimental to the obtention of low specific contact resistivity.

In addition to low contact resistivity and high transparency, an optimal ESC should also present a low recombination current. To assess such property, we have measured and analyzed the excess lifetime of the minority carrier. Fig. 1 (b) presents a schematic of the structure used to measure photoconductance by the quasi-steady state mode. The back side is passivated by depositing an a-Si:H stack (~15 nm), while on the front side, TiO_x was deposited.

The first strategy was to deposit the TiO_x film just as we did for the C&S structure, i.e., a previous HF cleaning was done to eliminate the native oxide. The results are depicted in Fig. 12 (a) for the 150 °C oxidation. As a reference, another sample without TiO_x (i.e., a-Si:H/c-Si (n)/SiO_x(native) structure) was measured, and we obtained a carrier lifetime of 39.7 μs and *i*Voc of 0.583 V. Once the TiO_x was deposited a low minority carrier lifetime of only 7.8 μs was measured. We performed some consecutive annealing processes on a hot plate to passivate the defects without controlling the process atmosphere. The temperatures used were kept below 300 °C to reduce the degradation of the a-Si:H layer on the rear side. At higher temperatures, hydrogen inside the a-Si:H could effuse, and thus, the passivation could be compromised. Besides, in the literature, some of the best passivation ALD TiO_x results were obtained within the 250 °C – 320 °C annealing range [53,54]. The lifetime showed a marginal improvement of 11 μs for an injection level of 10^{15} cm^{-3} with a 300 °C 5 min annealing. We also tested forming gas annealing (FGA) at 300 °C 5 min. This process aimed to introduce H to the film, which can diffuse to the interface and passivate the dangling bonds. However, we could not increase this lifetime value for this sample over 20.4 μs and an *i*Voc of 0.556V (at 10^{15} cm^{-3}). The results obtained for the 200 °C oxidation process were very similar.

Another approach that has been performed with TiO_x and MoO_x is the growth of a passivating chemical SiO_x [53,55] as a capping layer, this chemically grown SiO_x has been considered of better quality than the oxide that spontaneously grows during sputtering. We decided to test the chemical SiO_x growth by RCA clean, which produces a SiO_x thickness comparable to the one obtained by direct sputtering of TiO_x, ~2 nm. Thus, no HF cleaning was performed on these samples before introducing them into the HPS chamber to preserve the chemically grown SiO_x. The lifetime results of this approach are depicted in Fig. 12 (b). Again, as a reference, we consider the sample without TiO_x that was described in the previous paragraph. After depositing the TiO_x film, we obtained values of 9.5 μs and 0.547 V. This reduction shows that the

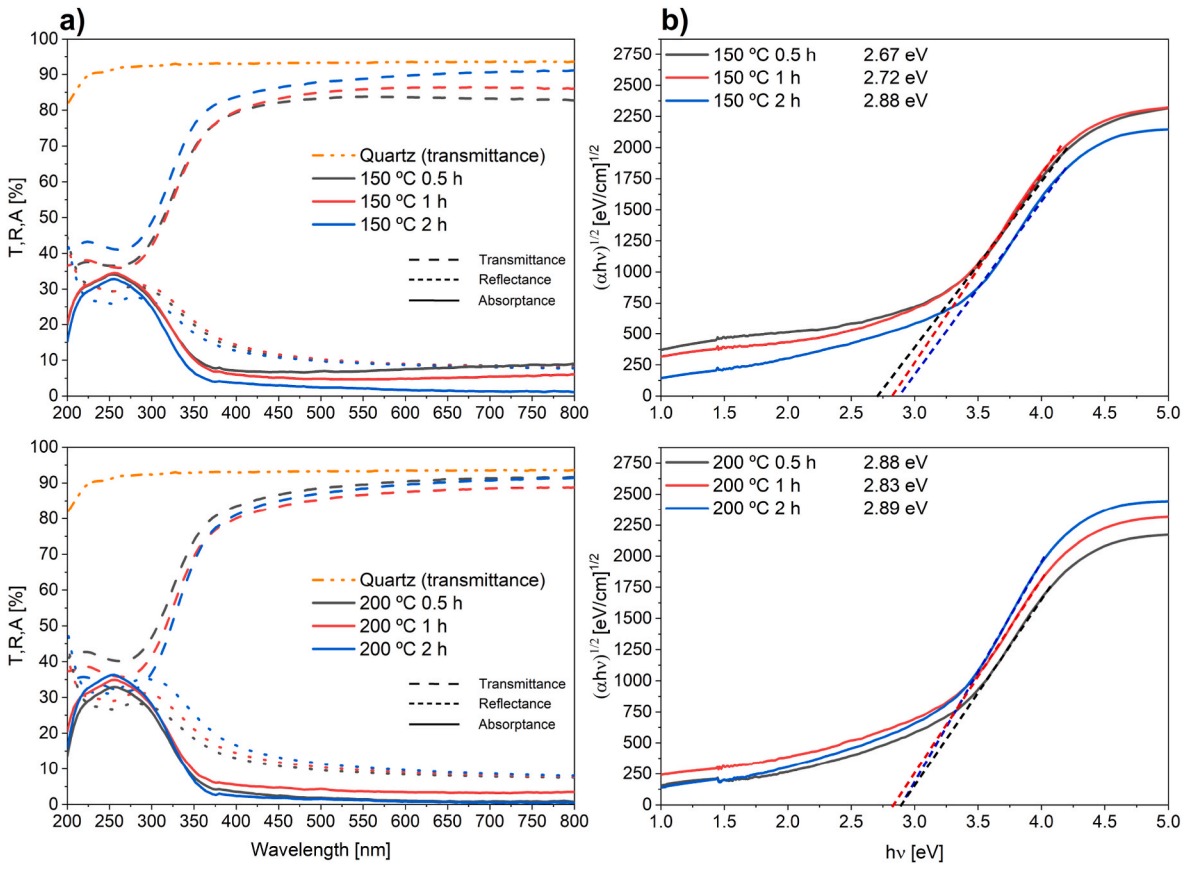

Fig. 11. a) T-R-A curves for TiO_x layers deposited on quartz and b) Tauc's plot for obtaining the optical band gap of the same samples.

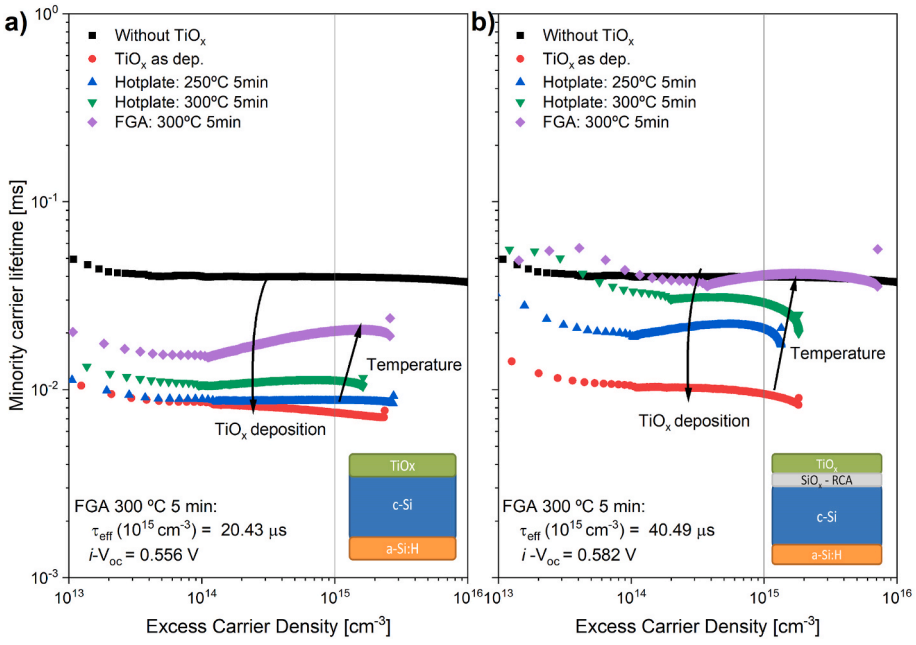

Fig. 12. Carrier lifetime measurements obtained by QSS-PC for a) a-Si:H/c-Si/TiO_x structure and b) a-Si:H/c-Si/SiO_x (RCA)/TiO_x. For both samples, the TiO_x layer was deposited by the 2-step process ~4 nm Ti + oxidation process 150 °C 1h.

quality of the TiO_x as deposited is not good yet. However, after some annealing processes, the lifetime is recovered with a value of 40.49 μs and *i*Voc of 0.582 V. As previously mentioned, each annealing process was done in a subsequent manner. We used annealing processes below 300 °C to mitigate hydrogen effusion within the a-Si:H layer. This result suggests that the low lifetime issue can be improved by using better passivation layers.

4. Conclusions

This study presents the structural, optical, and electrical properties of TiO_x thin films deposited by HPS. A novel approach involving Ti deposition followed by low-temperature plasma oxidation (150 °C – 200 °C) was explored for ESC layers. XPS, FTIR, and TEM confirmed the successful oxidation of Ti layers with sub-stoichiometric TiO_x (Ti/O ~1.9). GIXRD showed that films oxidized at 150 °C were amorphous, while those at 200 °C displayed anatase TiO_x peaks. The 2-step oxidation process minimized Si oxidation, reducing contact resistivity (ρc), with values of 40 ± 27 mΩ cm^2 for 150 °C and 20 ± 29 mΩ cm^2 for 200 °C oxidation. The films exhibited high transmittance (>87 %) and optical band gaps of 2.67–2.88 eV for the 150 °C oxidized samples and 2.8 eV for the 200 °C oxidized samples. However, even after annealing, carrier lifetime measurements in a-Si:H/c-Si/TiO_x structures were insufficient for high-efficiency solar cells. The growth of a chemical SiO_x by the RCA process shows an improvement compared to native oxide. But still, FGA at 300 °C 5 min is necessary for achieving the best results for this process (40 μs at 10^{15} cm^{-3}). This indicates that the use of passivation capping layers improves minority carrier lifetime. Thus, we can conclude that the main limitation was carrier recombination at the TiO_x/Si interface.

The results show that HPS is a promising technique for obtaining ESC with low contact resistivity. The 2-step oxidation process presents a novel approach to fabricating TiO_x that allows the modification of the properties of the film as the oxidation parameters are modified (i.e., the time and temperature). Future work will focus on enhancing lifetime by incorporating alternative low-temperature passivation layers, such as evaporated SiO_x or PECVD a-Si:H, while maintaining low ρc and high transparency. The reduced sputtering damage due to high pressure is expected to minimize the degradation of passivating layers. This concern is what typically discourages the use of sputtering for selective contact deposition.

CRediT authorship contribution statement

F. Pérez-Zenteno: Writing – original draft, Methodology, Investigation, Formal analysis, Data curation. **E. García-Hemme:** Writing – review & editing, Supervision, Project administration, Methodology, Investigation, Funding acquisition, Formal analysis, Conceptualization. **I. Torres:** Writing – review & editing, Investigation, Formal analysis. **R. Barrio:** Writing – review & editing, Investigation, Formal analysis. **S. Duarte:** Writing – review & editing, Investigation. **R. Benítez-Fernández:** Writing – review & editing, Investigation. **D. Caudevilla:** Writing – review & editing, Investigation, Formal analysis. **R. García-Hernansanz:** Writing – review & editing, Investigation, Formal analysis, Conceptualization. **J. Olea:** Writing – review & editing, Investigation. **D. Pastor:** Writing – review & editing, Investigation. **A. del Prado:** Writing – review & editing, Project administration, Investigation, Funding acquisition. **E. San Andrés:** Writing – review & editing, Writing – original draft, Supervision, Project administration, Methodology, Investigation, Funding acquisition, Formal analysis, Data curation, Conceptualization.

Declaration of generative AI and AI-assisted technologies in the writing process

During the preparation of this work the author(s) used *DeepL Translate* in order to translate some difficult parts of the manuscript from Spanish to English. After using this tool/service, the author(s) reviewed and edited the content as needed and take(s) full responsibility for the content of the publication.

Declaration of competing interest

The authors declare that they have no known competing financial interests or personal relationships that could have appeared to influence the work reported in this paper.

Acknowledgments

The authors acknowledge the “CAI de Técnicas Físicas” of Universidad Complutense de Madrid (UCM) for ion implantation, RTA annealing and e-beam evaporation. “Centro de espectroscopía y correlación” of UCM for the FTIR measurements, the “CAI de difracción de Rayos X″ of UCM for the GIXRD measurements, surface characterization lab from CENIM-CSIC for the XPS analysis, CNME for the TEM images and XEDS measurements. Authors acknowledge the use of instrumentation and the technical advice provided by the National Facility ELECMI ICTS, node “Laboratorio de Microscopías Avanzadas" at University of Zaragoza. This project was funded by projects PID2020-116508RB-I00, TED2021-130894B-C21, PID2020-117498RB-I00, PID2023-149369OB, and PID2023-148178OB-C21 from the Spanish AEI, F. Pérez-Zenteno acknowledges UCM for the predoctoral (call CT58/21 – CT59/21). R. Benítez-Fernández acknowledges the research contracts under the Investigo Program (CT19/23-INVM-27) of the Ministerio de Trabajo y Economía Social.

Appendix A. Supplementary data

Supplementary data to this article can be found online at https://doi.org/10.1016/j.mssp.2024.109038.

Data availability

Data will be made available on request.

References

[1] A.R. Zanatta, et al., The Shockley–Queisser limit and the conversion efficiency of silicon-based solar cells, Results Opt 9 (November) (2022) 100320, https://doi.org/10.1016/j.rio.2022.100320.
[2] H. Lin, et al., Silicon heterojunction solar cells with up to 26.81% efficiency achieved by electrically optimized nanocrystalline-silicon hole contact layers, Nat. Energy 8 (8) (2023) 789–799, https://doi.org/10.1038/s41560-023-01255-2.
[3] Z.C. Holman, et al., Current losses at the front of silicon heterojunction solar cells, IEEE J. Photovoltaics 2 (1) (2012) 7–15, https://doi.org/10.1109/JPHOTOV.2011.2174967.
[4] T.N. Nguyen, et al., Memory characteristics of poly-Si using MIC as an active layer on glass substrates, J. Phys. D Appl. Phys. 43 (10) (2010), https://doi.org/10.1088/0022-3727/43/10/105406.
[5] J. Ibarra Michel, et al., Carrier-selective contacts using metal compounds for crystalline silicon solar cells, Prog. Photovoltaics Res. Appl. (2022), https://doi.org/10.1002/PIP.3552.
[6] L.G. Gerling, et al., Characterization of transition metal oxide/silicon heterojunctions for solar cell applications, Appl. Sci. 5 (2015) 695–705, https://doi.org/10.3390/app5040695.
[7] M. Mirsafaei, et al., Sputter-deposited titanium oxide layers as efficient electron selective contacts in organic photovoltaic devices, ACS Appl. Energy Mater. 3 (1) (2020) 253–259, https://doi.org/10.1021/acsaem.9b01454.
[8] M. Shahiduzzaman, et al., Spray pyrolyzed TiO 2 embedded multi-layer front contact design for high-efficiency perovskite solar cells, Mano-Micro Lett (2021), https://doi.org/10.1007/s40820-020-00559-2.
[9] G. Budiutama, et al., Effective passivation of TiO2/Si by interlayer SiOx controlled by scanning zone annealing for perovskite/Si tandem solar cell, Sol. Energy 236 (November 2021) (2022) 772–781, https://doi.org/10.1016/j.solener.2022.03.056.
[10] X. Yang, et al., Silicon heterojunction solar cells with electron selective TiOx contact, Sol. Energy Mater. Sol. Cells 150 (Jun. 2016) 32–38, https://doi.org/10.1016/J.SOLMAT.2016.01.020.
[11] K. Gotoh, et al., Tuning the electrical properties of titanium oxide bilayers prepared by atomic layer deposition at different temperatures, Phys. Status Solidi Appl. Mater. Sci. 216 (22) (2019) 1–5, https://doi.org/10.1002/pssa.201900495.

[12] V. Titova, et al., Effective passivation of crystalline silicon surfaces by ultrathin atomic-layer-deposited TiOx layers, Energy Proc. 124 (Sep. 2017) 441–447, https://doi.org/10.1016/J.EGYPRO.2017.09.272.
[13] X. Yang, et al., High-Performance TiO 2-based electron-selective contacts for crystalline silicon solar cells, Adv. Mater. (2016), https://doi.org/10.1002/adma.201600926.
[14] C. Lee, et al., Properties of thermally evaporated titanium dioxide as an electron-selective contact for silicon solar cells, Energies 13 (3) (2020) 1–10, https://doi.org/10.3390/en13030678.
[15] V. Matkivskyi, et al., Electronic-beam evaporation processed titanium oxide as an electron selective contact for silicon solar cells, Curr. Appl. Phys. 32 (September) (2021) 98–105, https://doi.org/10.1016/j.cap.2021.10.005.
[16] S. Fernández, et al., Sputtered ultrathin TiO2 as electron transport layer in silicon heterojunction solar cell technology, Nanomaterials 12 (14) (Jul. 2022) 2441, https://doi.org/10.3390/nano12142441.
[17] A. Eberst, et al., Advanced physics research deeper insight into the mechanisms behind sputter damage in silicon solar cells based on the example of nanocrystalline silicon carbide, Adv. Physics Res. 2400036 (2024), https://doi.org/10.1002/apxr.202400036.
[18] M. Bivour, et al., Comparison of low damage sputter deposition techniques, AIP Conf. Proc. 2147 (2019), https://doi.org/10.1063/1.5123836.
[19] U. Walter, Fundamentals of leybold vacuum technology, Vac. Handb. 199 (2007) [Online]. Available: https://www.leyboldproducts.com/media/pdf/87/a8/be/FVT_Fundamentals_of_Vacuum_Technology_EN58774555441f3.pdf.
[20] E.S. Andrés, et al., Physical properties of high pressure reactively sputtered TiO2, J. Vac. Sci. Technol. A Vacuum, Surfaces, Film. 23 (6) (Nov. 2005) 1523–1530, https://doi.org/10.1116/1.2056554.
[21] M. Toledano-Luque, et al., Hafnium oxide thin films deposited by high pressure reactive sputtering in atmosphere formed with different Ar/O2 ratios, Mater. Sci. Semicond. Process. 9 (6) (2006) 1020–1024, https://doi.org/10.1016/j.mssp.2006.10.018.
[22] Z. Gao, et al., Effects of Gd2O3 gate dielectric on proton-irradiated AlGaN/GaN HEMTs, IEEE Electron. Device Lett. 38 (5) (2017) 611–614, https://doi.org/10.1109/LED.2017.2682795.
[23] M.A. Pampillón, et al., High-k gadolinium scandate on Si obtained by high pressure sputtering from metal targets and in-situ plasma oxidation, Semicond. Sci. Technol. 32 (3) (2017), https://doi.org/10.1088/1361-6641/aa58cc.
[24] F.J.P. Zenteno, et al., High pressure sputtering of Mo targets in mixed Ar/O2/H2Atmospheres for hole selective contacts in photovoltaic cells, in: 14th Spanish Conf. Electron Devices, CDE 2023 - Proc., 2023, pp. 7–10, https://doi.org/10.1109/CDE58627.2023.10339461.
[25] C. Schinke, et al., Uncertainty analysis for the coefficient of band-to-band absorption of crystalline silicon, AIP Adv. 5 (6) (2015) 1–22, https://doi.org/10.1063/1.4923379.
[26] A. Jolivet, et al., Structural, optical, and electrical properties of TiO2 thin films deposited by ALD: impact of the substrate, the deposited thickness and the deposition temperature, Appl. Surf. Sci. 608 (July 2022) (2023), https://doi.org/10.1016/j.apsusc.2022.155214.
[27] C.D. Wagner, et al., Empirical atomic sensitivity factors for quantitative analysis by electron spectroscopy for chemical analysis, Surf. Interface Anal. 3 (5) (1981) 211–225, https://doi.org/10.1002/sia.740030506.
[28] B. van Wijngaarden, et al., Inaccuracies in contact resistivity from the Cox–Strack method: a review, Sol. Energy Mater. Sol. Cells 246 (2022) (2022), https://doi.org/10.1016/j.solmat.2022.111909.
[29] J.E. Sansonetti, W.C. Martin, Handbook of basic atomic spectroscopic data, J. Phys. Chem. Ref. Data 34 (4) (2005) 1559–2259, https://doi.org/10.1063/1.1800011.
[30] M.Á. Pampillón Arce, Growth of high permittivity dielectrics by high pressure sputtering from metallic targets, PhD thesis, in: Dep. Of Apply Physics III, Universidad Complutense de Madrid, 2017, pp. 64–73 [Online], http://link.springer.com/10.1007/978-3-319-66607-5.
[31] M. Arif, C. Eisenmenger-Sittner, In situ assessment of target poisoning evolution in magnetron sputtering, Surf. Coating. Technol. 324 (2017) 345–352, https://doi.org/10.1016/j.surfcoat.2017.05.047.
[32] Y.L. Jeyachandran, et al., Properties of titanium thin films deposited by dc magnetron sputtering, Mater. Sci. Eng. 431 (1–2) (2006) 277–284, https://doi.org/10.1016/j.msea.2006.06.020.
[33] Y. Ju, et al., Electrical properties of amorphous titanium oxide thin films for bolometric application, Adv. Condens. Matter Phys. 2013 (100) (2013) 1–5, https://doi.org/10.1155/2013/365475.
[34] W.C. Peng, et al., Tunability of p- and n-channel TiOx thin film transistors, Sci. Rep. 8 (1) (2018) 1–12, https://doi.org/10.1038/s41598-018-27598-5.
[35] P. Babelon, et al., SEM and XPS studies of titanium dioxide thin films grown by MOCVD, Thin Solid Films 322 (1–2) (1998) 63–67, https://doi.org/10.1016/S0040-6090(97)00958-9.
[36] B. Bharti, et al., Formation of oxygen vacancies and Ti 3+ state in TiO 2 thin film and enhanced optical properties by air plasma treatment, Sci. Rep. 6 (2016), https://doi.org/10.1038/srep32355.
[37] J.O. Carneiro, et al., Compositional, optical and electrical characteristics of SiOx thin films deposited by reactive pulsed DC magnetron sputtering, Coatings 9 (8) (2019), https://doi.org/10.3390/coatings9080468.
[38] C.B. Samantaray, et al., Effect of post-deposition annealing on microstructural and optical properties of barium strontium titanate thin films deposited by r.f. magnetron sputtering, J. Mater. Sci. Mater. Electron. 12 (7) (2001) 365–370, https://doi.org/10.1023/A:1011222312230.
[39] M.C. Marchi, et al., A comprehensive study of the influence of stoichiometry on the physical properties of TiOx films prepared by ion beam deposition, J. Appl. Phys. 108 (6) (2010) 64912, https://doi.org/10.1063/1.3481442.
[40] S. Duēas, et al., A comparative study of the electrical properties of TiO2 films grown by high-pressure reactive sputtering and atomic layer deposition, Semicond. Sci. Technol. 20 (10) (2005) 1044–1051, https://doi.org/10.1088/0268-1242/20/10/011.
[41] M. Schnabel, et al., Self-assembled silicon nanocrystal arrays for photovoltaics, Physica Status Solidi (A) Applications and Materials Science 212 (8) (2015) 1649–1661, https://doi.org/10.1002/pssa.201431764.
[42] M. Shirolkar, et al., Rapidly switched wettability of titania films deposited by dc magnetron sputtering, J. Phys. D Appl. Phys. 41 (15) (2008), https://doi.org/10.1088/0022-3727/41/15/155308.
[43] M. Van Rijnbach, et al., On the accuracy of the cox-strack equation and method for contact resistivity determination, IEEE Trans. Electron. Dev. 67 (4) (2020) 1757–1763, https://doi.org/10.1109/TED.2020.2974194.
[44] V. Titova, J. Schmidt, Selectivity of TiOx-based electron-selective contacts on n-type crystalline silicon and solar cell efficiency potential, Phys. Status Solidi Rapid Res. Lett. 15 (9) (2021) 1–8, https://doi.org/10.1002/pssr.202100246.
[45] S. Miyagawa, et al., Application of Bayesian optimization for high-performance TiOx/SiOy/c-Si passivating contact, Sol. Energy Mater. Sol. Cells 230 (June) (2021) 111251, https://doi.org/10.1016/j.solmat.2021.111251.
[46] D. Augustowski, et al., Magnetron sputtered electron blocking layer as an efficient method to improve dye-sensitized solar cell performance, Energies 13 (11) (2020), https://doi.org/10.3390/en13112690.
[47] Y. Doubi, et al., Experimental study of properties of TiO2 thin films deposited by spray pyrolysis for future sensory applications, Appl. Phys. Mater. Sci. Process 127 (6) (2021) 1–11, https://doi.org/10.1007/s00339-021-04629-z.
[48] J. Klein, et al., Limitations of the Tauc plot method, Adv. Funct. Mater. 33 (47) (2023) 1–19, https://doi.org/10.1002/adfm.202304523.
[49] B. Zhou, et al., Preparation and characterization of TiO2 thin film by thermal oxidation of sputtered Ti film, Mater. Sci. Semicond. Process. 16 (2) (Apr. 2013) 513–519, https://doi.org/10.1016/j.mssp.2012.05.001.
[50] A. El Mesoudy, et al., Band gap narrowing induced by oxygen vacancies in reactively sputtered TiO2 thin films, Thin Solid Films 769 (February) (2023) 139737, https://doi.org/10.1016/j.tsf.2023.139737.
[51] R.V. Nair, et al., A review on optical bandgap engineering in TiO2nanostructures via doping and intrinsic vacancy modulation towards visible light applications, J. Phys. D Appl. Phys. 55 (31) (2022), https://doi.org/10.1088/1361-6463/ac6135.
[52] R.V. Nair, et al., Large bandgap narrowing in rutile TiO2 aimed towards visible light applications and its correlation with vacancy-type defects history and transformation, J. Phys. D Appl. Phys. 51 (4) (2018), https://doi.org/10.1088/1361-6463/aaa187.
[53] K. Gotoh, et al., Passivation mechanism of the high-performance titanium oxide carrier-selective contacts on crystalline silicon studied by spectroscopic ellipsometry, Jpn. J. Appl. Phys. 60 (SB) (2021), https://doi.org/10.35848/1347-4065/abd6dd.
[54] Y. Nakagawa, et al., Effect of forming gas annealing on hydrogen content and surface morphology of titanium oxide coated crystalline silicon heterocontacts, J. Vac. Sci. Technol. A Vacuum, Surfaces, Film. 38 (2) (2020), https://doi.org/10.1116/1.5134719.
[55] J. Tong, et al., Impact of pregrown SiO x on the carrier selectivity and thermal stability of molybdenum-oxide-passivated contact for Si solar cells, Cite This ACS Appl. Mater. Interfaces 13 (2021) 36435, https://doi.org/10.1021/acsami.1c06765.